TOPICAL REVIEW — Low-dimensional nanostructures and devices

Controllable growth of low-dimensional nanostructures on well-defined surfaces*

Qin Zhi-Hui(秦志辉)†

State Key Laboratory of Magnetic Resonance and Atomic and Molecular Physics, Wuhan Institute of Physics and Mathematics, Chinese Academy of Sciences, Wuhan 430071, *China*

(Received 27 June 2013)

The controllable growth of nanostructures with desired geometric order and well-defined shapes has stimulated great interest due to its applicability in the development of microelectronic devices. Self-assembly is an efficient and versatile way to guide the atoms or molecules into low-dimensional nanostructures as a consequence of balancing complex interplay between adsorbate-adsorbate and adsorbate–substrate interfacial interactions. The tailoring of low-dimensional nanostructures by control of inter-adsorbate and adsorbate–substrate interfacial interactions is reviewed. Such inherent interactions greatly influence not only the size and shape of the growing nanostructures, but also their chemical identity. The degree of interaction between adsorbates can be controlled via preparation procedures, opening up the study of the influence of this phenomenon with respect to reactivity and catalytic behavior. The formation of well-defined molecular layers can be controlled not only by repulsive molecule-molecule interaction but also by symmetry matching or charge transfer between adsorbed molecules and the substrate. It has become obvious that inter-adsorbate and adsorbate–substrate interfacial interactions can be tuned to fabricate diverse surface nanostructures from semiconductor, metallic, and molecular materials.

Keywords: nanostructures, self-assembly, intermolecular interactions, scanning tunneling microscopy

PACS: 81.07.–b, 81.16.Dn, 87.15.hg, 68.37.Ef **DOI:** 10.1088/1674-1056/22/9/098108

1. Introduction

Low-dimensional structures have stimulated great interest because they often exhibit unique electronic and optical properties that differ from those observed in corresponding bulk materials.[1] For example, one-dimensional (1D) nanostructured materials with a high aspect ratio, such as nanorods/nanowires, have dimensionality-dependent and size reduction-dependent electrical and thermal transport or mechanical properties.[2,3] Zero-dimensional nanoparticles have special catalytic or magnetic properties originating from surface and quantum size effects. These properties are closely related to the average number of atoms in the particle or the equilibrium shape of the particle.

Enormous efforts have already been made to tailor nanostructures with desired geometric order and well-defined shapes. There are two different strategies for creating nanostructured materials in a controllable and repeatable manner: "top-down" and "bottom-up" techniques.[4] The former exemplified by extreme ultraviolet or even hard X-ray lithography,[5] electron-beam writing, or microcontact stamping,[6] can only create nanostructures down to the sub-100-nm range.

Another way is used to efficiently guide the atoms or molecules into nanometer-scale structures through the assembly process.[7] Usually, atomic or/and molecular constituents are deposited onto a solid surface and the assembly of nanostructures is the consequence of complex interplay between adsorbate–adsorbate and adsorbate–substrate interfacial interactions. On a homogeneous surface inter-adsorbate interaction controls the adsorbed species, forming geometric pattern with equivalent binding sites. For example, on metallic surfaces, the strong attractive force between adsorbed metal atoms results in the formation of compact two-dimensional (2D) and three-dimensional (3D) islands.[8] While between organic molecules, the repulsive or attractive forces generally lead to the growth of well-ordered superstructures in registry with the lattice of the substrate.[9–16] Actually, on solid surfaces, the potential landscape for adsorption is unavoidably perturbed by point or line defects, which greatly influences the spatial distribution of the adsorbates.[17] Additionally, by inserting an epitaxial layer between the adsorbates and the metallic substrate, the underlying metallic states are effectively decoupled and the adsorbate–substrate interaction is weakened.[18,19] Due to the lattice mismatch between the epitaxial layer and the metal substrate, electronic superstructures form within the epitaxial layer, which leads to inhomogeneous distribution of the adsorbate–substrate interaction.[20–25] Moreover, the tunability of charge transfer from the metal substrate to the adsorbed atomic or molecular constituents by directly tunneling through the nano-patterned superstructure layer may be an additional

*Project supported by the National Natural Science Foundation of China (Grant No. 11004219) and the National Basic Research Program of China (Grant No. 2013CBA01600).

†Corresponding author. E-mail: zhqin@wipm.ac.cn

© 2013 Chinese Physical Society and IOP Publishing Ltd

factor that influences the inter-adsorbate interaction and then the mode of spatial distribution/growth of the metal nanoparticles or organic molecules.[25,26]

In this article, the growth of various low-dimensional nanostructures on well-defined surfaces will be reviewed with reference to our recent STM-based studies. In Section 2, the formation of low-dimensional nanostructures under the influence of a strong adsorbate–substrate interaction will be addressed, e.g., semiconductor-supported Ge nanoparticles or indium nanowires. In Section 3, nanostructural assemblies dominated by inter-adsorbate interactions and charge transfer-modulated electronic structures will be presented. Molecular nanostructures controlled by balancing complex interplay between adsorbate-adsorbate and adsorbate–substrate interfacial interactions will be discussed in Section 4. Section 5 concludes the article.

2. Assembly dominated by adsorbate–substrate interaction

STM investigation of coverage- and temperature-dependent structural evolution of Ge-based and indium-based nanostructures forming on Si(111) or Ge(001) is reviewed to elucidate the strong adsorbate–substrate interaction-dominated assembly of nanostructures. Encapsulation of the metal deposits induced by strong metal-support interactions will also be addressed.

2.1. Ge/Si(111)-7×7: From isolated atom to zero-dimensional nanoparticles to 2D nanostructures

Based on the commonly accepted Dimer–Adatom–Stacking (DAS) model,[27] each Si(111)-7×7 unit cell contains a large number of distinct bonding sites distributed in one faulted half unit cell (FHUC) and one unfaulted half unit cell (UHUC) with different reactivity, which makes this periodic surface an ideal template for growing well-ordered nanostructures. Ordered arrays of nanodots/nanoparticles, including Na,[28] Tl,[29] In,[30,31] Sn,[31–33] Cu,[34] Si,[35,36] Au,[37] and Pb,[38–40] have been fabricated successfully on this surface. Because of potential applications in unique microelectronic and optoelectronic devices, Ge-based nanostructures on the Si(111)-7×7 surface have been intensely studied,[36,41–45] and it has been treated as model system to investigate the evolution of self-assembly of various nanostructures as functions of coverage and annealing temperature.

To facilitate the formation of ordered Ge-based nanostructures on the Si(111)-7×7 surface, the substrate should be kept at temperature ranging from 100 to 300 °C during deposition, since at temperatures lower than 100 °C the physically deposited Ge atoms do not have enough mobility to span the dimer wall after arriving on the surface.[46–48] Figure 1(a) shows the STM topographic image of the initial Ge adsorption (0.10 ML) on Si(111)-7×7 surface at 150 °C. The individual Ge atoms substitute for Si adatoms, residing at a position higher by 0.2 Å than the original Si adatom (Fig. 1(b)), and preferentially occupy the corner Si adatom sites in FHUC with the correlated type-B pattern dominating (Figs. 1(c)–1(e)).[49]

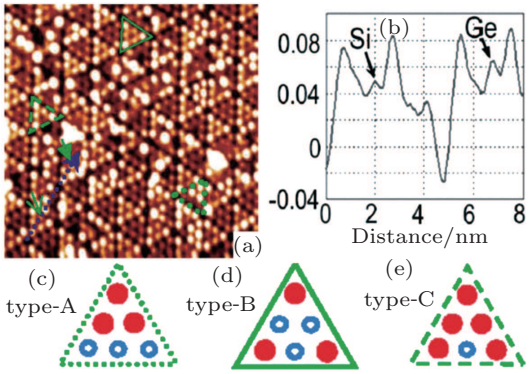


Fig. 1. (a) STM image (−1.5 V, 0.2 nA, 20 nm×20 nm) of Si(111)-7×7 surface with Ge coverage of 0.10 ML.[49] Three different configurations of Ge-correlated patterns are denoted by the dotted-line, solid-line, and dashed-line triangles. (b) The height profile corresponding to the dashed-arrow line in (a). Schematics for the three typical Ge-correlated patterns, named type A (c), type B (d), and type C (e), are also shown.[49]

With increasing coverage, isolated Ge nanoparticles with varying geometric configurations appear on the Si(111)-7×7 surface as shown in Fig. 2. Most of the Ge nanoparticles reside at the center of FHUCs, just fitting with FUHCs.[50] A higher substrate temperature during the deposition process greatly enhances the average mobility of the additional atoms, resulting in Ge nanoparticles with more uniform size and a preference of locating in FUHCs. Four configurations of Ge nanoparticles appearing in the same image suggest that the Ge nanoparticles evolve from triangular to tetragonal, then to pentagonal, and finally to a hexagonalstar-like structure.[50]

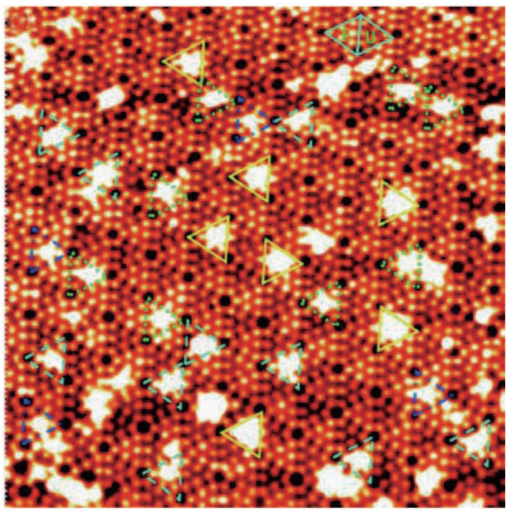


Fig. 2. STM image (2.0 V, 0.3 nA, 30 nm×30 nm) of Si(111)-7×7 surface covered by 0.12 ML Ge.[50] Ge nanoparticles with four typical geometrical configurations (triangular, tetragonal, pentagonal, and hexagonal) are denoted by triangles with the dot-dashed line, dotted line, dashed line, and solid line, respectively.[50]

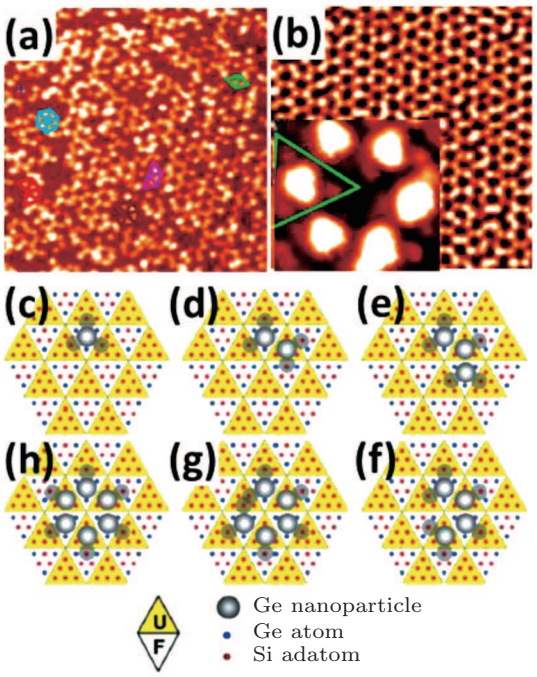


Fig. 3. STM images of Ge/Si(111)-7×7 at different Ge coverages. (a) 0.4 ML (2.2 V, 50 nm×50 nm).[51] (b) 0.5 ML (2.6 V, 50 nm×50 nm).[51] Six distinct patterns of the complexes of Ge nanoparticles, ranging from an isolated Ge nanoparticle to a pair of nanoparticles, an open nanoparticle ring, and finally a closed nanoparticle ring with six nanoparticles surrounding the hole (inset of Fig. 3(b)), are distinguished in panel (a) and simply depicted in panels (c)–(h), respectively.[51]

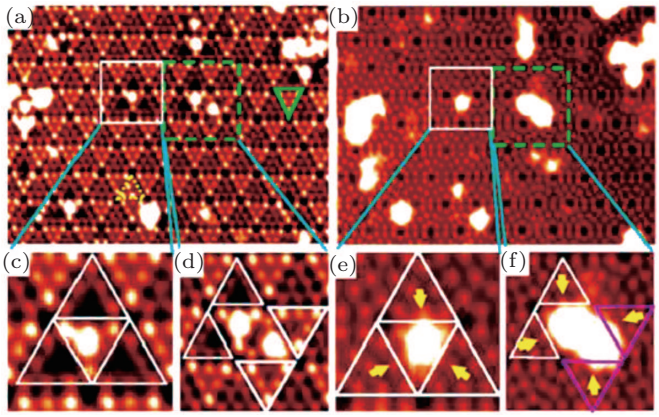


Fig. 4. (a) Filled-state and (b) empty-state STM images of Si(111)-7×7 after depositing 0.12 ML Ge.[51] (c)–(f) Close-up images for the two characteristic patterns and the nearby areas in panels (a) and (b).[51] The Si adatoms that are invisible in panels (c) and (d) are indicated by the arrows in panels (e) and (f).[51]

Further increasing deposition coverage leads to a gradual increase in the density of Ge nanoparticles with their distribution becoming very regular. As shown in Fig. 3(a), the complexes of Ge nanoparticles vary from an isolated pattern to hexagonal one as the initial dispersing arrangement evolves to the final ordered hexagonal network (Fig. 3(b)). The evolution of the complexes of Ge nanoparticles is sustained by charge transfer.[51] When an isolated Ge nanoparticle is formed in an FHUC (Fig. 3(c)), as shown in the filled-state STM image (Fig. 4(a)), the closest center Si adatoms in the nearest-neighbor UHUCs are invisible (Figs. 4(c) and 4(d)). From the corresponding empty-state STM image (Figs. 4(e) and 4(f)), the existence of the sead atoms excludes the geometric effect. The substantial depletion of electron density associated with these three Si adatoms suggests that electrons are transferred to the nearby Ge nanoparticle.[51] As local coverage increases, when a new nanoparticle forms in a neighboring UHUC, electrons are transferred from the two new surrounding FHUCs (Fig. 3(d)). First-principles calculations confirm the depletion of charge associated with the dangling bonds of the central Si adatoms in the three UHUCs surrounding a Ge nanoparticle in an FHUC (Fig. 3(c)) and the decrease in electronic energy that results from the charge transfer. The energy gain can be attributed to "local Madelung energy" which is used in determining the energy of a single ion in a crystal. The substantial reduction in the Madelung energy is used to overcome the factors that inhibit the formation of isolated nanoparticles in UHUCs, and the residual Madelung energy stabilizes the pair. Starting with a pair in adjacent FHUC and UHUCs, the third Ge nanoparticle tends to form in one of the FHUCs near the first two, accompanied by charge transfer from the nearby Si adatoms in adjacent half unit cells.[51] In this way, the fourth (Fig. 3(f)), fifth (Fig. 3(g)), and sixth nanoparticles (Fig. 3(h)) gradually form, eventually resulting in a hexagonal structure. The reduction of the local Madelung energies contributes to the stabilization of the local nanostructures.[51]

Deposition of Ge atoms on Si(111)-7×7 at room temperature (RT) followed by annealing to ∼300 °C or even higher temperature results in formation of 2D epitaxial Ge wetting layers. Figure 5(a) shows the STM image of one Ge-induced reconstruction coexisting with the Si(111)-7×7 reconstruction. From the neighbor–neighbor distance of Ge atoms (inset of Fig. 5(a)) and the angle between the main direction of the formed local reconstruction and the boundary of the nearby 7×7 unit cells, Ge-induced 2D nanoscale structures were determined to be $(\sqrt{3}\times\sqrt{3})R30^\circ$ with respect to the bulk 1×1 structure.[52] Direct deposition of Ge atoms on Si(111)-7×7 kept at ∼ 300 °C also leads to formation of Ge-induced 2D $(\sqrt{3}\times\sqrt{3})R30^\circ$ nanostructures, as shown in Fig. 5(b). From the first-principles density-functional calculations, one can learn that Ge atoms preferentially occupies the T_4 sites on the unreconstructed Si(111) substrate as shown in the inset of Fig. 5(b). During the growth of this nanostructure, the surface Si atoms will rearrange to the bulk 1×1 structure.[53] Different energy barriers must be overcome for removing reconstruction in the UHUCs and FHUCs (the energy barrier is relatively lower in UHUCs than in FUHCs[54]). Therefore, the activation barrier for Ge overgrowth in the FHUCs is clearly higher than in the UHUCs. Thus, the $(\sqrt{3}\times\sqrt{3})R30^\circ$ nanostructure is surrounded by FHUCs, as shown in Fig. 5(b).

Upon deposition of Ge atoms on Si(111)-7×7 kept at ~300 °C, triangular epitaxial Ge islands consisting of domains of 7×7 and 5×5 periodic reconstruction were also formed, as shown in Figs. 5(c) and 5(d).[46,50] The intermixing of Ge/Si plays an important role in the epitaxial growth of these Ge islands.[55]

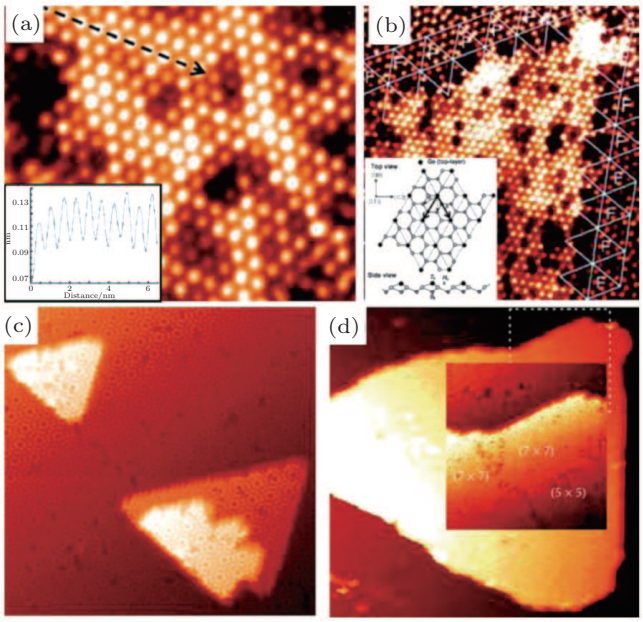


Fig. 5. (a) High-resolution STM image (1.6 V, 0.20 nA, 12 nm×10 nm) of the 2D nanostructure formed on Si(111) with a Ge coverage of 0.30 ML after annealing at 300 °C.[52] Inset: the height profile along the dashed line indicated in (a).[52] (b) Close-up STM image (1.4 V, 0.20 nA, 22 nm×29 nm) of the Ge-induced 2D nanostructures obtained by direct deposition of Ge on Si(111) kept at 300 °C.[50] Inset: top and side views of the schematic arrangement for reconstruction with the adatoms at the T_4 sites. The solid circles represent the adatoms. Larger open circles and smaller ones are for the Si atoms in the first and second layers, respectively.[52] (c) and (d) STM images show typical Ge islands on the Si(111)-7×7 substrate formed upon direct deposition of Ge on Si(111) kept at 300 °C. (c) 45 nm×45 nm, 2.0 V, 0.10 nA.[46] Two-dimensional Ge triangular epitaxial islands have the same orientation as the nearby Si(111)-7×7 reconstruction. (d) 120 nm×100 nm, 1.8 V, 0.15 nA.[50] Inset: close-up STM image (45 nm×45 nm, 1.2 V, 0.15 nA) shows 7×7 and 5×5 reconstructions coexisting inside the Ge island.[50]

2.2. In/Ge(001): From 1D nanowires to faceted indium nanoparticles

Nanostructured materials with high aspect ratios such as nanorods and nanowires often exhibit anisotropic electronic and optical properties that differ from those observed in the bulk materials, and these properties have been given much attention due to their potential applications in microelectronic and optoelectronic devices.[4,7,56] Due to the ordered dimer-row (2×1) structure,[57,58] Ge(001) and Si(001) surfaces are good templates for fabricating 1D nanostructures via the "bottom-up" strategy.[59–64] Because no indium–germanium compounds have been found in the binary system, indium-based nanostructure/Ge(001) system has been a model system to investigate the evolution of self-assembled 1D metal nanowires with coverage and annealing temperature.[65–73]

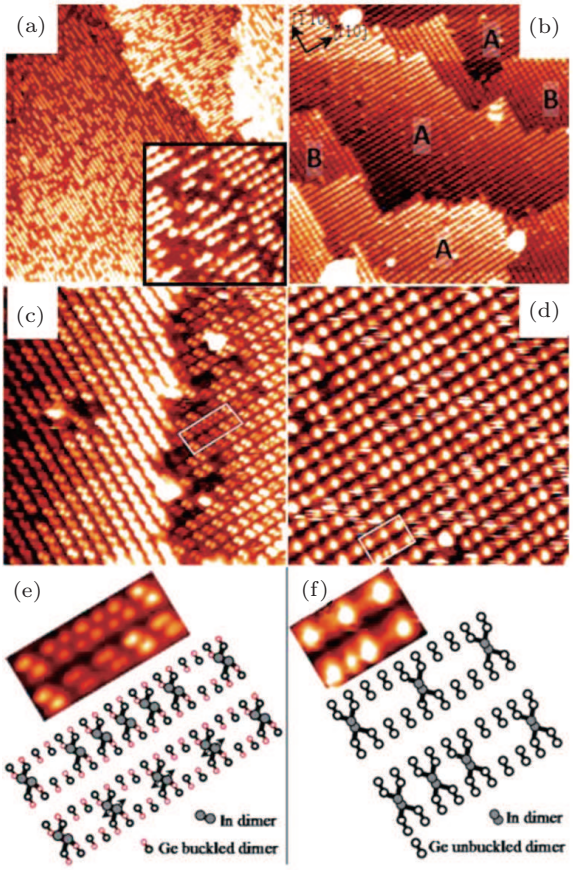


Fig. 6. (a) STM image (106 nm×106 nm, 1.50 V, 0.40 nA) of 0.85 ML indium on Ge(001) surface, deposited at RT and annealed at 320 °C for 1 h. The inset is its high resolution STM image (20 nm×20 nm, −1.10 V, 0.20 nA) on one terrace.[72] (b) STM image (71 nm×71 nm, −1.40 V, 0.30 nA) of 1.4 ML indium on Ge(001) surface, RT deposited and annealed at 320 °C for 1 h.[72] (c) and (d) High-resolution STM images obtained on two regions of (b).[72] (c) 34 nm×34 nm, −0.60 V, 0.30 nA; (d) 26 nm×26 nm, −0.60 V, 0.3 nA. (e) and (f) The structural models of In rows corresponding to the regions indicated by white rectangles.

A common feature for indium on Ge(001) is the 2×2 reconstruction consisting of parallel lines of dimerized indium adatoms.[68] Increasing coverage to 0.85 monolayer (1 ML= 1.3×10^{15} atoms·cm^{-2}) and subsequent annealing at 320 °C results in formation of In rows, which are made up of In dimers, lying between the substrate Ge dimer rows. As shown in Fig. 6(a), the assembled In rows have an equal spacing of 1.6 nm ($4a$), where a is the 1×1 substrate lattice constant. On adjacent terraces, In rows run perpendicularly in two directions [110] and [−110], respectively. Further increasing coverage to 1.4 ML, as shown in Fig. 6(b), results in fully covering the substrate by the assembled In rows, which still have equal spacing of 1.6 nm ($4a$). On any given terrace, In rows run parallel forming domain A (B). It is interesting that the In dimers making up the In rows exhibit different appearances in different regions, as shown in Figs. 6(c) and 6(d), respectively. It is known that on Ge(001) surface, the $c(4\times 2)$ structure corresponds to the ground state of the Ge(001) surface, and the transformation from $c(4\times 2)$ to the (2×1) structure occurs at 220–260 K.[73] At RT, because of thermal fluctuation, the dim-

mers undergo rapid flip–flop motions, exhibiting a symmetric (2×1) structure. Due to the strong bonding between the indium and the underlying germanium, the In dimers bonded with buckled Ge dimers also buckle, as shown in Fig. 6(e), and exhibit a protrusion as if bonded with unbuckled Ge dimer (Fig. 6(f)).

Upon deposition of 2.1-ML indium onto Ge(001) and followed by annealing at 130 °C, some indium nanoparticles with irregular shapes arbitrarily distribute among the In-row domain (Fig. 7(a)). Subjected to annealing, indium atoms in one domain first preferentially nucleate into small nanoparticles; subsequently, one side grows more rapidly than the other side, forming elongated nanoparticles, oriented in [010] and $[-100]$, running 45° counterclockwise from the direction of the In rows as shown in Fig. 7(b). This is an efficient way to relieve the strain. The elongated nanoparticles so formed are Ge{103}-faceted In nanoparticles, due to the fact that the four surfaces of the faceted In nanoparticles correspond to Ge(−103), (103), (0 − 13), and (013).[72] Further annealing treatment at 240 °C leads to the substrate being completely covered by Ge{103}-faceted In-nanoparticles (Fig. 7(c)). Upon further annealing at elevated temperature (320 °C, Fig. 7(d)), the average width and length of the Ge{103}-faceted In nanoparticles increase as more and more indium atoms locate on their surfaces.[72]

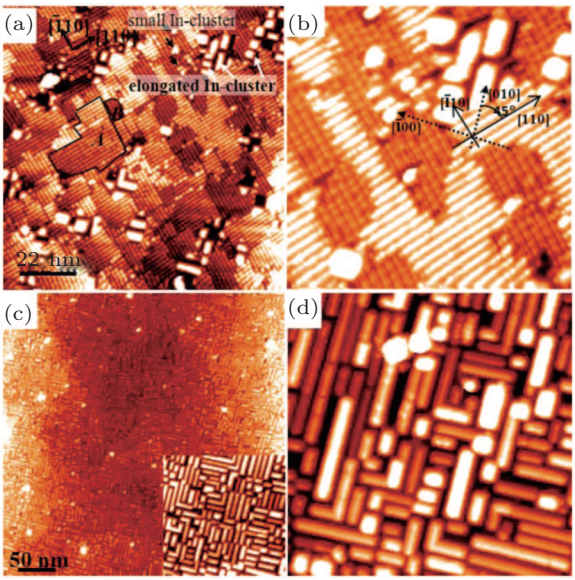


Fig. 7. (a) and (b) STM images (1.55 V, 0.30 nA) of the sample with 2.1 ML coverage of indium after 130 °C annealing for 1 h.[72] Scan scale is 110 nm×110 nm in panel (a) and 48 nm×48 nm in panel (b). Inset: relative orientations of the In rows and the Ge{103}-faceted In nanoparticles are indicated by the solid and dotted lines, respectively.[72] (c) Large scale Ge{103}-faceted In-nanoparticle topography (400 nm×400 nm, 1.40 V, 0.34 nA) of the sample (a) annealed at 240 °C for 1 h. Inset: zoomed-in STM image (100 nm×100 nm, 1.40 V, 0.34 nA).[72] (d) Typical STM image (100 nm×100 nm, 1.60 V, 0.34 nA) of the sample (c) after annealing at 320 °C for 1 h.[72]

2.3. Pt/Fe_3O_4/Pt(111): Strong metal-support interaction-induced encapsulation

Oxide supported metal nanoparticles, which are usually made of transition metals, play an important role in heterogeneous catalysis. The interaction between the metal nanoparticles and the underlying oxide greatly influences the growing nanoparticles not only their size and shape but also their chemical identity properties which are naturally correlated with their chemical performance.[74] It is generally accepted that deposition of metals with relatively high surface energy such as Pt, Rh, and Pd on oxides with relatively low surface energy such as titania, iron oxide, and ceria undergo the strong metal–support interaction (SMSI) effect.[75,76] Here, an STM study of Pt nanoparticles supported on Fe_3O_4(111) films is presented to provide evidence that the strong interaction between Pt and iron oxide induces encapsulation of Pt nanoparticles by the FeO monolayer upon annealing at elevated temperatures.[77,78]

The Fe_3O_4(111) films were grown on a Pt(111) substrate by depositing one monolayer of Fe onto clean Pt(111) at room temperature and subsequently oxidizing the sample in O_2 (10^{-6} mbar) at 1000 K for 2 min to form the FeO(111) monolayer film, followed by repeated cycles of ∼5 ML Fe deposition and oxidation at ∼900 K, with the final oxidation at ∼1000 K for 10 min. Figure 8(a) shows a typical STM image of the Pt/Fe_3O_4 (111) surface as deposited at 300 K.[78] After annealing at 600 K, as shown in Fig. 8(b), platinum forms extended 2D islands, ∼0.5 nm thick, that mostly exhibit irregular shapes, although some preferential orientation for the island edges can be seen. At the metal coverage studied (∼2.6 ML), 3D particles also form. Stepwise annealing to 850 K in UHV leads to an increase in particle size as shown in Fig. 8(d).[78] These annealed particles are well-faceted with a (111) top facet. Good metal/oxide epitaxy is observed as the particle edges are all parallel to the atomic rows on the Fe_3O_4(111) surface. It is clear that annealing induces Pt dewetting such that the Pt surface area decreases due to strong particle sintering with increasing annealing temperature. Corresponding CO TPD results demonstrate that stepwise annealing to 700 K and 800 K in UHV leads to a dramatic reduction of CO adsorption uptake, much more than the decrease in the Pt surface area upon sintering.[77] Considering that the capacity to adsorb CO is proportional to the Pt surface area, the suppression of CO adsorption clearly demonstrates the reduction of the Pt surface area with migration of oxide support material onto the Pt particles. The inset of Fig. 8(d) shows direct evidence for the encapsulation of Pt particles that the top facets of the largest particles exhibit a moiré superstructure with ∼25 Å periodicity. Since the moiré structure has the same periodicity as that of FeO(111) on Pt (111) (see Section 3.2 for details),[25,79,80] the encapsulating layer is clearly FeO(111) in nature.

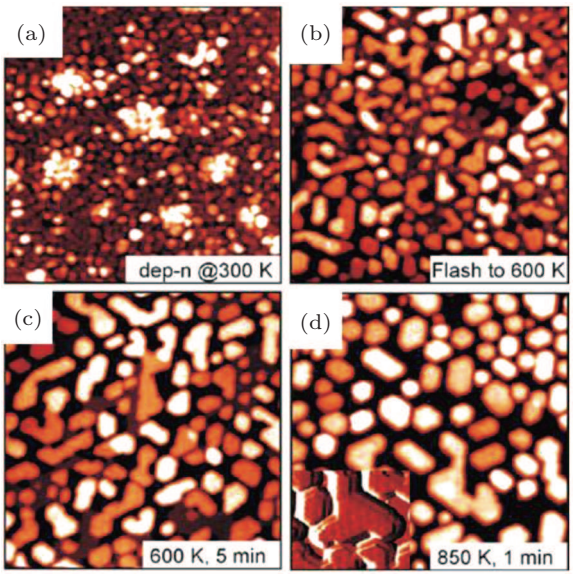


Fig. 8. STM images (100 nm×100 nm, 0.7 V, 0.4 nA) of 2.6 ML Pt deposited onto $Fe_3O_4(111)$ sample kept at 300 K (a) and after flashing to 600 K (b) and annealing at 600 K for 5 min (c) and at 850 K for 1 min (d).[78] The inset of (d) indicates the top facets of the Pt particles where the moiré superstructure is clearly resolved.[78]

The formation of Pt 2D structures on $Fe_3O_4(111)$ (Fig. 8(a)) implies a higher work of adhesion (W_{adh}), which is defined through the corresponding surface energies as

$$W_{adh} = \gamma_{oxide} + \gamma_{metal} - \gamma_{interface}. \quad (1)$$

The adhesion energy can be derived from the structural information on the basis of Wulff construction analysis of the particles with the equilibrium shape.[81,82] For Pt particles, mainly exposing (100) and (111) facets, the adhesion energy can be expressed as follows:

$$W_{adh} = \gamma_{111}\left(2 - \frac{3}{\sqrt{2}}\frac{s+1}{2s+1}\right), \quad (2)$$

where γ_{111} is the surface energy of the (111) surface, $h(w)$ is the height (width) of the nanoparticles, and s is the ratio of the top facet side length ($s = s_{100}/s_{111}$).

The irregularly shaped Pt 2D islands (see Figs. 8(b) and 8(c)) are not in an equilibrium shape and are in fact formed by the coalescence of smaller but better shaped ones. According to Eq. (2), for the small height/width ratios observed on Pt islands, the work of adhesion is rather insensitive to variations in s. By using the value of 2.3 J/m^2 for $\gamma_{Pt(111)}$,[83] the W_{adh} can be obtained as 4.0±0.5 J/m^2 even though there is a relatively large uncertainty.[77,78]

For 3D particles (Figs. 8(b) and 8(c)), the calculation is more precise and gives W_{adh} as 3.8±0.1 J/m^2. Both numbers are significantly larger than 3.15±0.1 J/m^2 for Pd/Fe_3O_4 (111) at 600 K and 3.25±0.3 J/m^2 previously found for Pd/alumina at 300 K.[82] For 3D particles (Fig. 8(d)), the same approach gives $W_{adh} = 4.15 \pm 0.1$ J/m^2 under the assumption that the particles expose clean Pt surfaces. The encapsulating oxide layer must reduce the surface energy of the particles formed at 850 K. In a crude approximation, γ_{111} must be replaced by γFeO/Pt(111) at 850 K. The latter is unknown but is obviously smaller than γPt(111). Therefore, the value 4.15 J/m^2 gives an upper limit in this case.[77] Thus, the above analysis shows that the strong interaction between Pt and Fe_3O_4 (111) leads to the encapsulation of Pt particles by an FeO(111) monolayer upon stepwise annealing, which is demonstrated in Fig. 9.

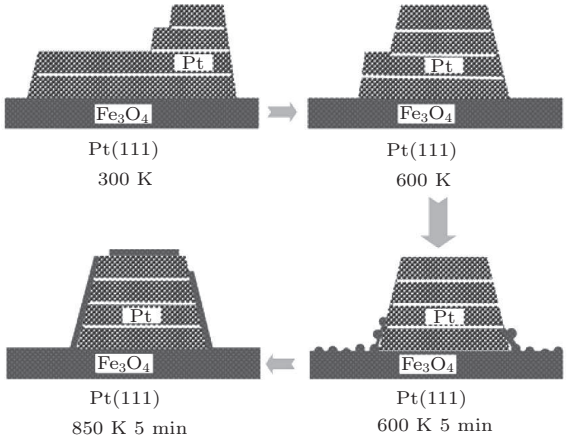


Fig. 9. The progress of SMSI-induced encapsulation of Pt particles by FeO monolayer upon stepwise annealing.

3. Assembly dominated by inter-adsorbate interaction

3.1. Pd, BaO/Al_2O_3/NiAl: Deposition sequence-influenced formation of bifunctional nanoparticles

As reported by Taglauer and Knözinger,[76] oxides with a relatively low surface energy (such as titania, ceria, iron oxide, and vanadia) undergo the SMSI effect, while alumina does not. On alumina, the degree of inter-adsorbate interaction can be controlled via the deposition sequence. In this section, the sequential co-deposition of bifunctional Pd/Ba oxide system on well-defined Al_2O_3/NiAl(110) was used as a model system. After reviewing the structure and growth behavior of the individual Pd and Ba nanoparticles on alumina, respectively, the inter-adsorbate interaction-dominated growth for the co-deposition systems have been found to be greatly influenced by the preparation procedure.

The Al_2O_3 film was produced by two cycles of oxidation of the NiAl(110) surface in 10^{-6} mbar O_2 at 550 K and subsequent UHV annealing at 1135 K. As shown in Fig. 10(a), on the obtained alumina film there are two types of domain boundaries, antiphase domain (APD) boundaries appearing as straight bright lines and rotational domain boundaries appearing as irregular lines.[17] Upon deposition of Ba and subsequent oxidation at 300 K, three-dimensional particles nucleate both on the domain boundaries and on the terraces with a high particle density estimated to be 5×10^{12}

particles·cm^{-2} (Fig. 10(b)), which points to a strong interaction with the support. A recent high-resolution photoelectron spectroscopy study shows that, even at RT, complete intermixing of Ba^{2+} and Al^{3+} ion occurs, leading to formation of $Ba_xAl_{2y}O_{x+3y}$ mixed oxide particles.[84] As shown in Fig. 10(c), Pd deposition after growth of the $Ba_xAl_{2y}O_{x+3y}$ particles leads to 3D aggregates with a high, homogeneous nucleation density ($\sim 3\times10^{12}$ particles·cm^{-2}) distributed over the entire surface.[85–87] The close-up (see inset of Fig. 10(d)) shows that between the majority of large aggregates, there is a second type of small aggregates with a lower density ($\sim 1\times10^{12}$ particles·cm^{-2}).

Compared to Pd deposition after growing the $Ba_xAl_{2y}O_{x+3y}$ particles, a very strong difference in nucleation behavior is observed for directly depositing Pd on pristine alumina film, as shown in Fig. 10(e). The formation of larger 3D nanoparticles preferentially nucleates at the rotational domain boundaries with density amounting to approximately 1×10^{12} particles·cm^{-2}. Palladium and Ba show very different nucleation and growth behaviors on the pristine support, with weak interaction and preferential nucleation at rotational domain boundaries for Pd, and strong interaction and high nucleation density for the Ba deposits. Based on the differences in the growth modes of the Pd and $Ba_xAl_{2y}O_{x+3y}$ particles discussed above, the larger particles in Fig. 10(c) are attributed to Pd aggregates nucleating on the preexisted $Ba_xAl_{2y}O_{x+3y}$ particles, and the smaller protrusions to leftover $Ba_xAl_{2y}O_{x+3y}$ particles,which have not yet been covered by Pd.

After growth of the Pd particles, Ba deposition and subsequent oxidation results in two types of particles, shown in the corresponding STM images (Fig. 10(f)). On the basis of their typical nucleation behavior, the larger particles can be attributed to Pd particles that preferentially decorate the rotational domain boundaries. Between the Pd particles, there is a higher density of small aggregates nucleating both on alumina terraces and at domain boundaries, which are assigned to isolated $Ba_xAl_{2y}O_{x+3y}$ particles without direct contact to Pd. It is worth noting that the density of the isolated $Ba_xAl_{2y}O_{x+3y}$ particles is significantly lower ($\sim 2\times10^{12}$ particles·cm^{-2}) than for growth on the pristine alumina, which suggests that a substantial fraction of the Ba is collected by nucleating on the Pd particles.

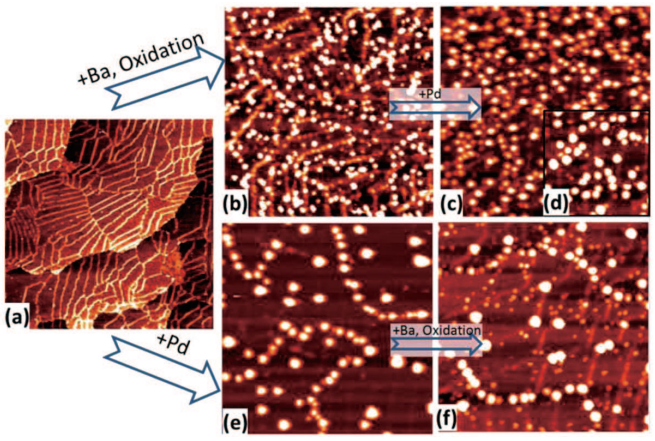


Fig. 10. (a) STM (100 nm×100 nm, 3.0 V, 0.15 nA) of the Al_2O_3/NiAl(110) model support showing the typical defect structures.[85] (b) STM (100 nm×100 nm, 2.7 V, 0.16 nA) after deposition of Ba and subsequent oxidation at 300 K.[86,87] (c) STM (100 nm×100 nm, 2.5 V, 0.17 nA) and (d) close-up (40 nm×40 nm, 2.5 V, 0.17 nA) image after deposition of Pd on $Ba_xAl_{2y}O_{x+3y}$/Al_2O_3/NiAl(110) prepared at 300 K (Fig. 1(b)).[86] (e) STM overview (200 nm×200 nm, 2.2 V, 0.17 nA) after deposition of Pd at 300 K on pristine Al_2O_3/NiAl(110) support.[86] (f) STM (100 nm×100 nm, 2.8 V, 0.15 nA) image after Ba deposition onto Pd/Al_2O_3/NiAl(110) and subsequent oxidation at 300 K.[86]

The different structure and growth behavior as a function of deposition sequence allows us to modify the interaction between barium aluminate-like and Pd nanoparticles supported on the Al_2O_3 film. The initial growth of $Ba_xAl_{2y}O_{x+3y}$ leads to formation of a high density of three-dimensional Pd particles nucleating at the pre-deposited barium aluminate aggregates, whereas the initial deposition of Pd gives rise to the formation of isolated $Ba_xAl_{2y}O_{x+3y}$ aggregates in addition to surface modified Pd particles. The degree of interaction between metal nanoparticles and oxide nanoparticles can be controlled via the preparation procedure, opening up the possibility to study the influence of this property with respect to reactivity and catalytic behavior.[88,89]

3.2. C_{60}/FeO/Pt(111): Charge transfer modulated electronic structures

The distribution of metal particles on oxide surfaces is not only largely determined by heterogeneous nucleation on defect sites,[90,91] but also influenced by the presence of electronic superstructures, as observed on thin Al_2O_3 films.[92] On polar oxide surfaces, spatial variation in the surface potential, which is built up by a modulated distance between the layers carrying an opposite net charge, would also influence the local arrangement of adsorbates.

For example, the Pt(111) supported FeO film has a bilayer structure with Fe adhering to the Pt(111) and O atoms forming the outermost layer.[93–97] The mismatch between the Fe–Fe distance ($\sim$ 3.10 Å) and the Pt–Pt distance ($\sim$2.73 Å) gives rise to a moiré pattern with a period of about 25.8 Å. According to their characteristic contrast (Figs. 11(a) and 11(b)) within the moiré cell, three kinds of regions are distinguished with fairly distinct stacking configurations (Fig. 11(c)). For example, at bias voltages of 4.5 V and above, the "atop" regions are imaged as bright protrusions, which had been attributed to the local variations in the energy at which field-emission resonances happen.[20,98–101] From the atomically resolved STM image (Fig. 11(b)), the alignment of the oxygen atoms rotates about 5.8° relative to the lattice of the moiré cell as depicted in Fig. 11(c). Additionally, due to the positive charge of the iron layer and the negative charge of the oxygen layer, a surface dipole is built up perpendicular to the surface

plane. The separation between the iron layer and the oxygen layer modulates in different regions, resulting in the spatial variations of the surface potential within the moiré cell.[20,97]

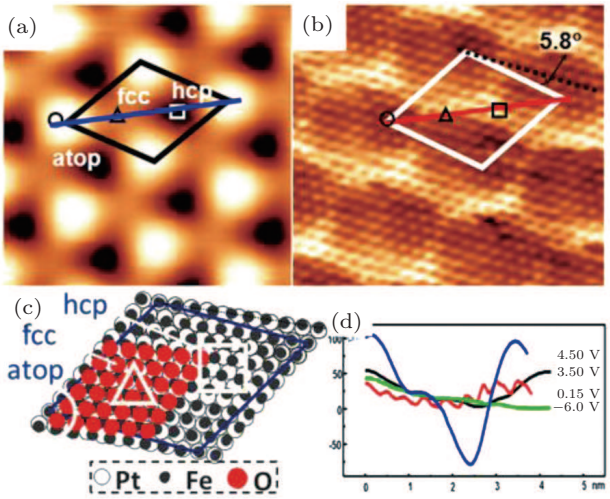


Fig. 11. (a) Moiré pattern (8 nm×8 nm, 4.50 V, 40 pA) of the FeO/Pt(111) film.[25] (b) Corresponding atomic resolution image (8 nm×8 nm, 0.15 V, 55 pA) of the FeO film.[25] The moiré cell is denoted by parallelograms. (c) The proposed structure of the FeO layer on Pt(111).[25,93] Only a portion of the oxygen atoms are shown. (d) Line profile across the atop, fcc and hcp regions of the moiré cell obtained at different bias voltages.[25]

C_{60}-based compounds and/or assembly have stimulated much physical and technical interest for their unique electronic properties and significant physical characteristics.[102–105] In the majority of practical applications, the formation of homogeneous C_{60} structure greatly improves the performance of the device.[106,107] Moreover, this ordering is important in understanding the molecule–environment interaction.[108,109] The physical behaviors and/or properties of C_{60}–metal systems depend on the nature of the chemical bond (which is related to the orientations of the C_{60} cage), on their geometric adsorption structures, and on the partial filling of the lowest unoccupied molecular orbital (LUMO) which is influenced by the charge transfer from the supported metal. Herein, the exploitation of the above-mentioned FeO layer on Pt(111) as a template will be reviewed, with special attention to the fact that the inhomogeneous distribution of the work function within the FeO layer tunes the degree of charge transfer between the C_{60} molecules and the Pt(111), resulting in the formation of the final C_{60} superstructures and/or superlattice.

As reported previously, due to the work function variation (as much as 0.4 eV[20]), organic molecules and metallic nanoparticles are highly site-selective inside the FeO moiré cell at lower temperatures.[21,22] Here, as demonstrated in Fig. 12(a), the C_{60} molecules assemble into compact molecular islands at sample temperature of 400 K. The formation of compact C_{60} island indicates the C_{60}–C_{60} interaction is stronger than the C_{60}–FeO interaction. C_{60} molecules prefer to nucleate and align with the moiré lattice of the underlying FeO layer. Since the FeO layer effectively reduces the hybridization of the C_{60} molecular frontier orbitals with the wave functions of the underlying Pt(111), C_{60} molecules exhibit various internal molecular structures and orientations. As shown in the empty-state STM image (Fig. 12(b)), the majority of C_{60} molecules present a dumbbell pattern, which corresponds to the C_{60} molecule with a 6:6 bond facing up.[16,19] Two other configurations are also identified: hexagonal ring facing up (hexagon) and a1 (one lobe brighter than the other two). Such varied molecular configurations might be caused by different bonding geometries on the oxide layer. The configuration of the C_{60}molecules periodically varies and a kind of regular C_{60}/FeO (111)-$(\sqrt{133}\times\sqrt{133})R17.5°$ structure forms.[25]

The electronic structure of the C_{60} molecular layer is found to be influenced by the spatially distributed electronic

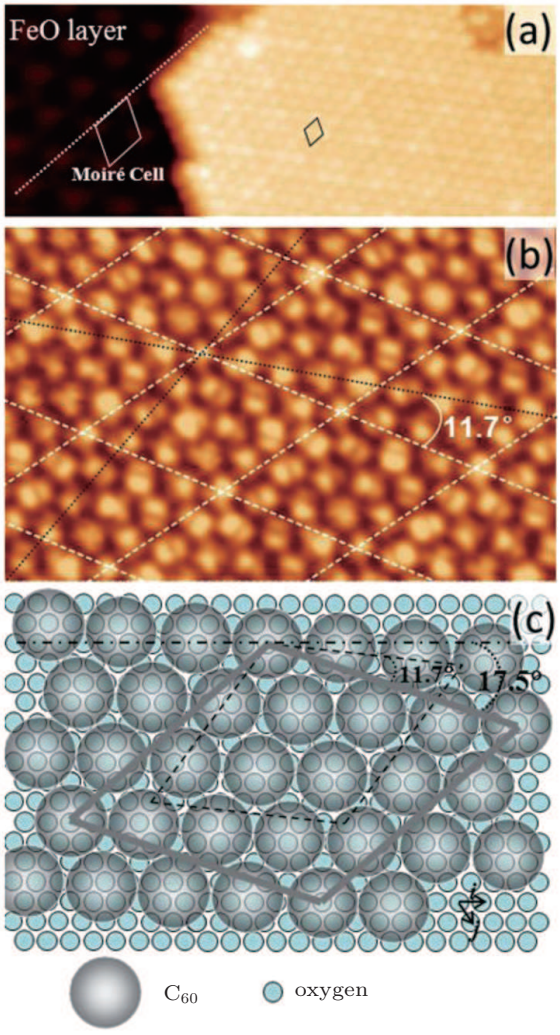


Fig. 12. (a) Morphology (30 nm×11 nm, 3.50 V, 20 pA) of FeO/Pt(111) after deposition of less than 1 ML C_{60} fullerenes.[25] (b) Orientationally ordered commensurate coincidence superstructure (15 nm×12 nm, 3.50 V, 48 pA) of C_{60} molecules on FeO/Pt(111).[25] Three configurations are distinguished in the STM image: 6:6 bond facing up, hexagonal ring facing up, and a1 (one lobe brighter than the other two). (c) Structure diagram for the C_{60} molecular $(\sqrt{133}\times\sqrt{133})R17.5°$ orientation ordering, in which big balls represent the position of C_{60} molecules, neglecting molecular orientation. For clarity, only the outermost oxygen layer of the underlying FeO layer is shown and one moiré cell is indicated by a dashed parallelogram.[25]

states of the underlying polar FeO layer. Figures 13(a)–13(d) demonstrate filled-state STM images of the same assembled C_{60} molecular layer with distinct appearances. For empty-state STM scanning (Fig. 12(b)), there is no difference in the molecular contrast with changing bias voltage. For filled-state STM scanning (Fig. 13), the bright-dim molecular contrast is bias-dependent. Moreover, with increasing bias voltage, the molecular contrast becomes more obvious and finally reaches an apparent height difference of 0.40 Å at −5.0 V. Dim-bright molecular contrast has been found in C_{60} monolayer on Cu(111),[109] on Ag(100),[110] and on Cu(100),[111,112] and has been interpreted as a topographic feature attributed to C_{60}-induced substrate reconstruction. Here, the dim-bright contrast (0.40 Å) is likely to be associated with the molecular electronic effect rather than a geometric effect.[25] Similarly, for C_{60} on Pb(111), two kinds of moiré structures with different angles relative to the Pb symmetry direction were shown to arise from electronic effects.[26]

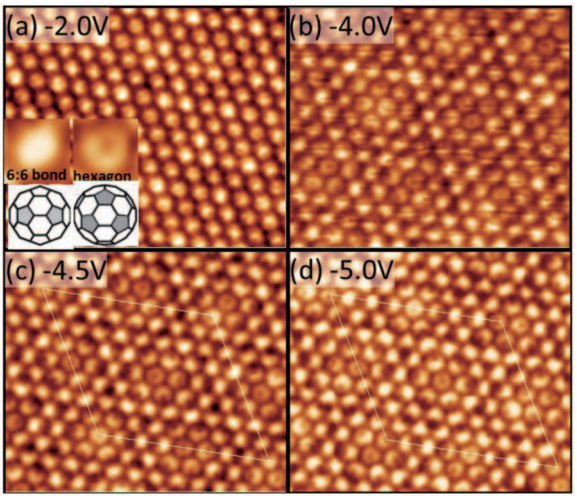


Fig. 13. STM images of the same region (12 nm×10 nm, 20 pA) obtained with different bias voltages, as indicated in the image.[25] The C_{60} molecular contrast shows bias dependence. Coincidence 8×8 superstructure with respect to the C_{60} primitive cell is marked by parallelograms in panels (c) and (d).

Upon C_{60} adsorption on a Pt(111)-supported FeO layer, charge could transfer between the Pt(111) surface and the C_{60} molecules by tunneling through the thin oxide layer. Due to the inhomogeneous distribution of the work function, the magnitude of charge transfer may be tuned when C_{60} resides in different regions. One can speculate that electrons prefer to transfer from the Pt(111) to the electron-attracting C_{60} cage. The direction of the charge transfer may also be influenced by the dipole orientation of the oxide layer underneath. Anyway, because of the modulated degrees of the charge transfer, C_{60} molecules possess different electronic states when residing on different regions, and they exhibit bright-dim STM contrast. As shown in Figs. 13(c) and 13(d), the majority of C_{60} molecules are imaged as protrusions, and the rest are shown up as a protrusion with a hole. According to density function theory (DFT) calculations,[19] the C_{60} molecules exhibiting bright protrusions in the filled-state STM image are oriented with a 6:6 bond facing up, and the protrusions with a hole correspond to molecular orientations with a hexagonal ring facing up. By considering the commensurability between the C_{60} N–N distance and the underlying moiré lattice, one more likely coincidence lattice ordering would be a $p(8\times8)$ structure with respect to the C_{60} primitive cell, which overlays a 3×3 moiré cell of the FeO layer.

4. Assembly by delicate balance between inter-adsorbate and adsorbate–substrate interactions

The adsorption of organic molecules on metal surfaces has been intensively studied for prospective applications in electronic and optoelectronic devices.[113–117] Because effective π–π stacking of organic molecules can greatly facilitate the overlapping of their π orbitals, resulting in high carrier mobility, formation of homogeneously ordered molecular structures can greatly improve the performance of the moletronic devices.[118] In general, molecular ordering on a surface is precisely governed by a delicate balance between intermolecular and molecule–substrate interactions.[9–14] In particular, metal phthalocyanines (MePcs) and fullerenes have attracted remarkable interest, in hope of applying them in fabricating moletronic devices, especially in the field of gas and radiation sensors,[119–122] hydrogen storage and spin-based quantum computing devices.[102,104,123]

Here, we choose two typical molecules, the CoPc molecule with planar π-conjugate structure and C_{60} with spheroidal π-conjugate structure. As we know, the intermolecular and molecule–substrate interactions can be controlled, to some extent, by the symmetry of the substrate. Due to the symmetry match between fcc(001) metal surfaces and MePc molecules, it can be expected that well-defined self-assembly MePc layers could be formed on these surfaces. In Section 4.1, on a selected substrate, Cu(001), the evolving molecular orientations and structures of CoPc molecules from disordered distribution, to self-assembled monolayer (SAM), and finally periodic structures in the second layer are reviewed. The coverage-dependent structures and their evolutions dominated by competing intermolecular and molecule–substrate interactions will be discussed in detail.[15]

Several studies have indicated that the underlying surfaces may dramatically reconstruct upon fullerene adsorption.[124–126] Unlike the adsorption and growth of planar CoPc molecule, C_{60} adds an additional degree of freedom by molecular rotation, a characteristic which is crucial in

the understanding of the C_{60} growth manner. As we know, the binding geometry and the exact adsorption structure of the molecules on the surface may play an important role when measuring the conductance through a single molecule.[127–130] For C_{60}, the complex adsorption structures on metallic substrates depend on the nature of the chemical bond which is related to the orientations of the C_{60} cage with respect to the substrate, on their geometric adsorption structures, and on the partial filling of the lowest unoccupied molecular orbital (LUMO), which is influenced by the charge transfer from the substrate metal.[131,132] The work function of the substrate is an important factor for the amount of charge transferred to the C_{60} cage. To better elucidate the nature of the charge transfer-induced partial filling of the LUMO, Pt(111) substrate, with its higher work function, was adopted. Moreover, at a high enough temperature, the interaction between Pt(111) and C_{60} molecules is able to catalyze decomposition of the fullerene cage,[133,134] demonstrating the strong bonding between them. In Section 4.2, for the system of C_{60} on Pt(111),[16] the intramolecular orientations, interfacial structures, their adsorption structure transformation as functions of coverage and temperature as well as their thermal stability before decomposition will be reviewed in order to understand the interaction between C_{60} and its environment, an understanding that is fundamental to the development of C_{60}-based devices.

4.1. CoPc/Cu(001): Symmetry matching

Previous studies demonstrated that MePcs take various adsorption structures and orientations depending on the central metal ions and the substrate underneath.[135–138] Moreover, the electronic properties of MePcs can thus be greatly influenced as well. For example, the Kondo effect of MePcs was strongly influenced by the molecule–substrate interfacial interactions.[139–141] Since the adsorption sites and thereby the self-assembly manner of the MePcs are dominated by the molecule–molecule interaction (MMI) and molecule–substrate interaction (MSI), which vary with the molecular concentration, it is necessary to systemically investigate the coverage-dependent MePcs adsorption structures and their evolution. In this section, we review the competing intermolecular and molecule–substrate interactions dominated molecular orientations and structures of CoPc molecules on Cu(001) from disordered distribution, to self-assembled monolayer (SAM), and finally periodic structures in the second layer.[15]

Upon RT deposition, CoPc molecules separately distribute on the Cu(001) surface (Fig. 14(a)). CoPc molecules have a strong tendency to locate at the step sites of Cu(001), assembling into molecular chains along the step edges.[15] High resolution STM images (Figs. 14(b) and 14(c)) demonstrate that well-defined four-leaf-clover CoPc molecules are formed. The center Co^{2+} ions display as protrusions in the filled state (Fig. 14(b)) and as depressions in the empty state (Fig. 14(c)), which can be ascribed to the different Co^{2+} dz^2 orbital contribution to tunneling current at different bias polarity.[142] From Fig. 14(d), it is observed that the Co^{2+} lies directly on the top site of the Cu atom and the molecular lobes have an angle of $\pm 22.5^\circ$ with respect to the $[1\ -1\ 0]$ direction. From the sketched molecular adsorption configurations (Fig. 14(e)), the molecules showing two configurations have the same chemical environments and adsorption energy, and thereby have the equivalent adsorption ratio. No other adsorption configurations can be found, even when the coverage is increased to monolayer, which indicates that the CoPc molecules are stable in both adsorption configurations at RT. Upon increasing the coverage to 0.83 ML, as shown in Figs. 14(f) and 14(g), the molecules arrange into a quasi-hexagonal lattice, which can be proved by corresponding fast Fourier transform (FFT) (inset of Fig. 14(g)). The molecules randomly distribute in one domain with two different adsorption configurations (Fig. 14(e)) as clearly indicated by depicting molecular contours (Fig. 14(g)). In accord with the intermolecular spacing, the molecular adsorption structure is proposed in Fig. 14(h), in which the blue solid circles represent the positions of CoPc molecules, neglecting the orientation information, and the yellow ones represent the copper atoms underneath. As shown in Fig. 14(i), the CoPc molecules rarely adsorb on top of other CoPc molecules until monolayer coverage is reached. The lattice of the first layer is not quasi-hexagonal anymore, but assembles into a quadrate lattice as shown in Fig. 14(j). The corresponding molecular reconstruction structure is proposed as $(\sqrt{29} \times \sqrt{29})R21.8^\circ$, as shown in Fig. 14(k). Note that molecule insertion is possible in the quasi-hexagonal arrangement (Fig. 14(g)). With more CoPc molecules coming to the surface, molecule insertion induces the formation of the quadrate reconstruction, a more compact arrangement.[15] Comparing the 0.83 ML and 1.05 ML cases, in the latter case the molecules have consistent orientation induced by intermolecular interactions, in which the short-ranged intermolecular repulsive force dominates their assembly. As the molecular distance is short enough, the energy associated with the repulsive force can overcome the molecular rotation potential barrier, and the molecules rotate and form the quadrate lattice. The total energy of the system is lowered as a result of the consistent orientation. On the other hand, in the 0.83 ML case the CoPc molecules have a little longer intermolecular distance, and the repulsive force attenuates rabidly, resulting in inconsistent orientation in quasi-hexagonal arrangement.[15]

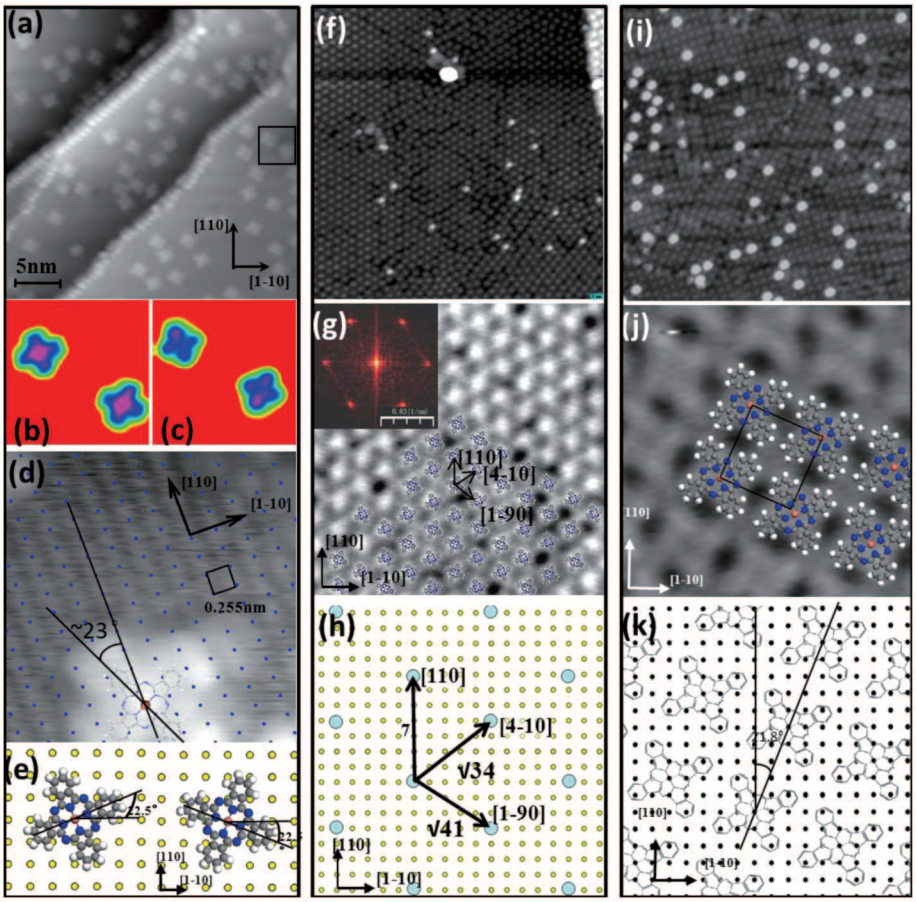


Fig. 14. (a) Typical STM image (30 nm×30 nm, 2.0 V, 59 pA) of CoPc molecules (∼0.20 ML) on Cu(001) surface.[15] (b) and (c) Zoomed-in STM images (5 nm×5 nm, 44 pA) of the region indicated by a solid square showing isolated CoPc molecules with different appearances.[15] (b) −0.50 V, (c) 1.50 V. (d) STM image with a CoPc molecule and the substrate lattice resolved simultaneously.[15] (e) Two equivalent adsorption structural models of CoPc on Cu(001).[15] (f) STM image of ∼0.83 ML CoPc on Cu(001) surface.[15] (g) Zoomed-in STM image (15 nm×15 nm, 1.0 V, 50 pA). Inset is the corresponding FFT image suggesting quasi-hexagonal molecular arrangement.[15] (h) Proposed reconstruction structure.[15] Yellow and blue spots represent the positions of the substrate copper atoms and the Co^{2+} ions of CoPc molecules, respectively. (i) STM image (50 nm×50 nm, 0.50 V, 50 pA) of CoPc with 1.05 ML coverage.[15] (j) Compact arrangement structure of the first molecular layer. (k) Proposed structural model for the CoPc monolayer on Cu(001).[15]

With molecular coverage increased to ∼1.6 ML, as shown in Fig. 15(a), the molecules of the second layer aggregate into a quadrate lattice but with a different lattice distance, which has been identified as $\sqrt{58} \times \sqrt{58}$ reconstruction.[15] On the surface, there are a few domains, such as one domain indicated by the arrow, in which the molecules arrange more compactly. From the zoomed-in STM image (Fig. 15(b)), it can be clearly seen that there are two kinds of molecular lattices. A corresponding schematic is shown in Fig. 15(c). The high-resolution STM images of the $\sqrt{58} \times \sqrt{58}$ superlattice (Fig. 15(d)) displays that every phenyl-lobe of CoPc adsorbed on top of the first CoPc layer changes into two fragments, relating to the free CoPc molecules orbital, and the central Co^{2+} ions are more pronounced, different from the molecules directly adsorbed on Cu(001) in appearance. All the molecules in both $\sqrt{58} \times \sqrt{58}$ and $\sqrt{29} \times \sqrt{29}$ constructions locate on top sites of the first layer. However, the molecules rotate 45° in the $\sqrt{58} \times \sqrt{58}$ structure while no rotation is found in the $\sqrt{29} \times \sqrt{29}$ structure. The different molecules–substrate interfacial and intermolecular interactions are supposed to play a key role for these orientation differences. At the initial period of molecular adsorption on the first layer, the molecules rotate 45° as mentioned in the 1.05 ML case. As more and more molecules adsorb on the first layer, first the molecules arrange into the $\sqrt{58} \times \sqrt{58}$ superlattice. Owing to the large intermolecular distance, a CoPc molecule can enter a $\sqrt{58} \times \sqrt{58}$ unit cell, as the molecular coverage is high enough, leading to the formation of $\sqrt{29} \times \sqrt{29}$ reconstruction. Figure 15(e) shows the possible structural evolution process from $\sqrt{58} \times \sqrt{58}$ structure to $\sqrt{29} \times \sqrt{29}$ structure. The insertion of a CoPc molecule into a $\sqrt{58} \times \sqrt{58}$ unit cell induces this molecule and its neighboring ones to rotate and form an angle of 0° with respect to the ones underneath, in order to decrease the energy of the whole system, forming the $\sqrt{29} \times \sqrt{29}$-$R$21.8° structure.[15]

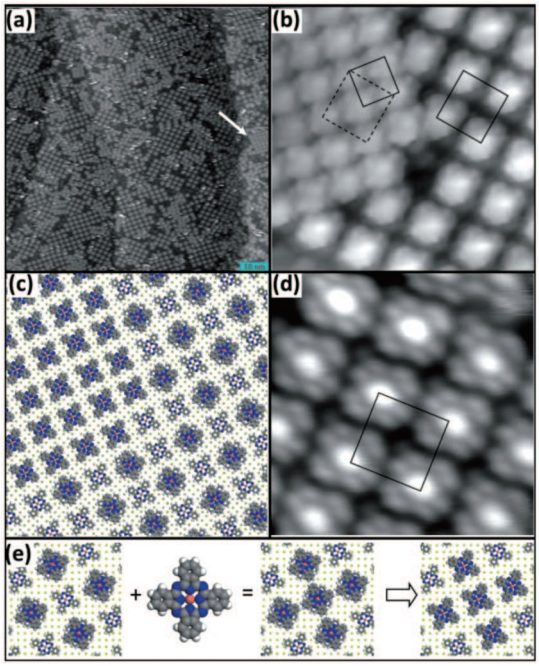


Fig. 15. (a) STM image (93 nm×93 nm, 2.05 V, 71 pA) of the surface with CoPc coverage of ∼1.6 ML.[15] (b) An area (9.25 nm×9.25 nm, 2.05 V, 72 pA) having both $\sqrt{58}\times\sqrt{58}$ and $\sqrt{29}\times\sqrt{29}$ structures and (c) is its schematic structure.[15] (d) High-resolution STM image (4.5 nm×4.5 nm) of the second molecular layer with $\sqrt{58}\times\sqrt{58}$ structure (1.50 V). (e) Proposed structural transition process from $\sqrt{58}\times\sqrt{58}$ to $\sqrt{29}\times\sqrt{29}$ structure.[15]

4.2. C_{60}/Pt(111): Charge transfer

Recently, a large number of studies have focused on the adsorption and interaction of C_{60} molecules with solid surfaces, in which a variety of C_{60}–substrate interactions, ranging from weak van der Waals type to strong chemisorptions have been revealed.[21–23,28,29,108,143–154] Due to the complex adsorption structures of C_{60} on metallic substrates, the nature of C_{60}–metal interactions is still far from being completely understood. The focus of this section is to review the thermally activated intra-molecular orientations and interfacial structural reconstructions as well as the transformation of their adsorption structure.

Upon RT deposition of C_{60} molecules on a Pt(111) surface, C_{60} aggregate into larger islands, as shown in Fig. 16(a). The corresponding line profile (not shown here) demonstrates the formation of C_{60} single-layer islands (SLIs), which is the consequence of balancing C_{60}–C_{60} intermolecular interaction and C_{60}–substrate interfacial interaction.[16] This growth mode is associated with the relatively low mobility of C_{60} molecules, as previously revealed for C_{60} on SiC nanomesh,[155] and is also consistent with the strong C_{60}–Pt interaction as predicted.[156–158] The C_{60} molecules form oriented domains, as denoted by *A* and *B*. The orientations of the two domains are rotated 15±1° with respect to the Pt⟨1 − 1 0⟩ direction. It is concluded that both domains (*A* and *B*) correspond to C_{60}/Pt(111)-$(\sqrt{13}\times\sqrt{13})R13.9°$ superstructure.

Orientations of C_{60} molecule with respect to Pt(111) are clearly identified in a high-resolution STM image (Fig. 16(b)). Rotations of C_{60} on Pt(111) are hindered at RT due to the strong molecule–substrate interaction/bond. Five types of molecular topographies are clearly revealed, among which 89% of the C_{60} molecules show the dumbbell pattern (6:6 bond), with their C_2 symmetry axis randomly oriented in the plane. Molecularly resolved STM images (Figs. 16(c) and 16(d)) reveal that stepwise thermal treatment induces C_{60} molecules to arrange into a more and more ordered orientation (Fig. 16(e)) with the final formation of a three-lobe intramolecular pattern as shown in Fig. 16(d).[16]

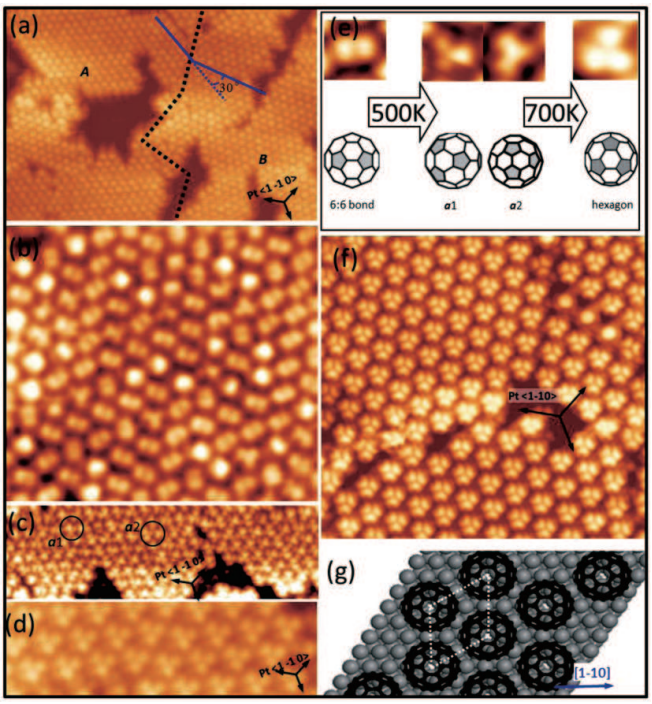


Fig. 16. (a) Molecular-resolution STM image (30 nm×25 nm) of C_{60} single layer (2.0 V, 30 pA).[16] (b) High resolution STM image (2.0 V, 40 pA, 12 nm×10 nm) of C_{60}SAM on Pt(111) with clearly resolved molecular orientations.[16] (c) High resolution STM image (2.0 V, 40 pA, 20 nm×7 nm) showing the molecular orientation after annealing treatment. Most molecules show 'a1' and 'a2' configurations that are randomly oriented. At the circled area, molecules in the same rows are oriented uniformly.[16] (d) Uniformly self-assembled C_{60} molecules with hexagonal configuration after further annealing of the sample at 700 K for 10 min (2.0 V, 40 pA, 10 nm×3 nm).[16] (e) The thermally activated evolution of molecular orientations in C_{60}SAM on Pt(111).[16] (f) High resolution STM image (2.0 V, 40 pA, 14 nm×14 nm) showing C_{60} molecules of C_{60}/Pt(111)-$(\sqrt{13}\times\sqrt{13})R13.9°$ (lower part) and $(2\sqrt{3}\times 2\sqrt{3})R30°$ domains (upper part) with ordered distribution and orientation.[16] (g) Proposed adsorption model of C_{60}/Pt(111) $(2\sqrt{3}\times 2\sqrt{3})R30°$ superstructure.[16]

Figure 16(f) displays a typical STM image of the sample subjected to further annealing at ∼1100 K.[16] The C_{60} molecules are resolved to have the identical molecular configuration (hexagon) within two $(2\sqrt{3}\times 2\sqrt{3})R30°$ domains (upper part) and a $(\sqrt{13}\times\sqrt{13})R13.9°$ domain (lower part) with some exception at the domain boundaries. That C_{60} molecules can stably exist on the Pt(111) surface after annealing at 1100 K suggests the strong bonding between C_{60}

and Pt surface atoms. In addition, from the high-resolution STM images, it can be seen that the molecular orientation and appearance are identical, adopting hexagonal configuration in C_{60}/Pt(111)-$(2\sqrt{3}\times 2\sqrt{3})R30^\circ$ and C_{60}/Pt(111)-$(\sqrt{13}\times\sqrt{13})R13.9^\circ$ domains, and three vectors of the hexagon face-up of all the C_{60} molecules are parallel to the Pt$\langle 1-10\rangle$ direction. Also, all the C_{60} molecules on Pt(111) have similar apparent heights. These phenomena suggest that the interfacial structure in C_{60}/Pt(111)-$(2\sqrt{3}\times 2\sqrt{3})R30^\circ$ domain is most probably the same as in C_{60}/Pt(111)-$(\sqrt{13}\times\sqrt{13})R13.9^\circ$ domain.[159] Figure 16(g) displays the corresponding proposed adsorption structure, following the C_{60}/Pt(111)-$(\sqrt{13}\times\sqrt{13})R13.9^\circ$ interfacial structure. First-principles calculations have demonstrated that C_{60} molecules adsorb on the Pt(111) surface with the center of a hexagonal ring located on top of a surface Pt atom. One Pt atom under every C_{60} molecule can be removed easily, and the neighboring slightly displaced Pt surface atoms form six covalent Pt–C bonds with the C_{60} molecular hexagonal faces.[160] The strong covalent bonds between C_{60} and the Pt(111) surface and the formation of adatom-vacancy pairs in the C_{60}/Pt(111) system may be the main driving forces promoting the substrate reconstruction pattern observed in experiments.[160]

5. Conclusion and outlook

Experiments with controlled growth of low-dimensional nanostructures on solid surfaces provide valuable information for the development of future nanoscale devices. In this review, we show that various nanostructures can be tailored with desired geometric order and well-defined shapes by balancing the interplay between adsorbate-adsorbate and adsorbate–substrate interfacial interactions. On template surfaces, such as Si(111)-7×7 and Ge(001)-2×1, ordered nanoparticles/nanowires can be formed under the domination of strong adsorbate–substrate interaction. For example, on Si(111)-7×7, diverse Ge-based nanostructures can be assembled as functions of coverage and annealing temperature, ranging from an isolated, substituted atom to "local Madelung energy" stabilized nanoparticles with varying geometric configurations and to a Ge/Si intermixing-induced 2D wetting layer. Moreover, the strong interaction between the metal nanoparticles and the underlying oxide support greatly influence not only the size and shape of the growing nanoparticles but also their chemical identity. For example, Pt nanoparticle encapsulation by FeO monolayer is induced by the SMSI effect. Additionally, by inserting an oxide layer between the adsorbate and the metallic substrate, the underlying metallicstates are effectively decoupled, making the adsorbate–substrate interaction weaker. The degree of interaction between nanoparticles can be controlled via the preparation procedure, thus opening up the possibility to study the influence of this property with respect to reactivity and catalytic behavior. Moreover, the charge transfer from the metal substrate to the adsorbed atoms or molecular constituents may be tuned by changing the spatial variations of the surface potential inside the polar oxide layer in order to influence the inter-adsorbate interaction and, in turn, the spatial distribution/growth mode of the metal nanoparticles or organic molecules. On metal surfaces, the adsorption sites and thereby the self-assembly mode of the adsorbed molecules are precisely governed by a delicate balance between intermolecular and molecule–substrate interactions. The formation of well-defined molecular layers can be controlled not only by the laterally repulsive molecule-molecule interaction but also by symmetry matching (e.g., CoPc on Cu(001)) or charge transfer between adsorbed molecules and the substrate (e.g., C_{60} on Pt(111)). We believe that these STM-based studies of tailoring low-dimensional nanostructures in a controlled manner are of great interest for further atomic scale engineering. A further challenge for the future would be to understand the nature of interactions between atoms or molecules or supermolecules within the assembled functional structures through a combination of advanced experimental techniques and first-principles calculations.

Acknowledgment

The author would like to thank those who have contributed to the project over the years, including H. J. Gao, H. J. Freund, G. Y. Cao, Y. L. Wang, H. M. Guo, S. Shaikhutdinov, H. F. Ma, D. X. Shi, S. W. Wang, S. T. Pantelides, Q. M. Guo, C. D. Liu, J. Chen, M. Huang, A. Desikusumastuti, M. Lewandowski, and J. Libuda, a necessarily incomplete list.

References

[1] Roduner E 2006 *Chem. Soc. Rev.* **35** 583
[2] Favier F, Walter E C, Zach M P, Benter T and Penner R M 2001 *Science* **293** 2227
[3] Yang F, Taggart D K and Penner R M 2009 *Nano Lett.* **9** 2177
[4] Gates B D, Xu Q, Stewart M, Ryan D, Willson C G and Whitesides G M 2005 *Chem. Rev.* **105** 1171
[5] Ito T and Okazaki S 2000 *Nature* **406** 1027
[6] Xia Y N, Rogers J A, Paul K E and Whitesides G M 1999 *Chem. Rev.* **99** 1823
[7] Barth J V, Costantini G and Kern K 2005 *Nature* **437** 671
[8] Stoldt C R, Cadilhe A M, Bartelt M C, Jenks C J, Thiel P A and Evans J W 1998 *Prog. Surf. Sci.* **59** 67
[9] Theobald J A, Oxtoby N S, Phillips M A, Champness N R and Beton P H 2003 *Nature* **424** 1029
[10] Du S X, Gao H J, Seidel C, Tsetseris L, Ji W, Kopf H, Chi L F, Fuchs H, Pennycook S J and Pantelides S T 2006 *Phys. Rev. Lett.* **97** 156105
[11] Forrest S R 1997 *Chem. Rev.* **97** 1793
[12] Barlow S M and Raval R 2003 *Surf. Sci. Rep.* **50** 201
[13] Shi D X, Ji W, Lin X, He X B, Lian J C, Gao L, Cai J M, Lin H, Du S X, Lin F, Seidel C, Chi LF, Hofer W A, Fuchs H and Gao H J 2006 *Phys. Rev. Lett.* **96** 226101
[14] Peumans P, Uchida S and Forrest S R 2003 *Nature* **425** 158
[15] Guo Q M, Qin Z H, Zang K, Liu C D, Yu Y H and Cao G Y 2010 *Langmuir* **26** 11804

[16] Liu C D, Qin Z H, Chen J, Guo Q M, Yu Y H and Cao G Y 2011 *J. Chem. Phys.* **134** 044707
[17] Schmid M, Shishkin M, Kresse G, Napetschnig E, Varga P, Kulawik M, Nilius N, Rust H P and Freund H J 2006 *Phys. Rev. Lett.* **97** 046101
[18] Repp J and Meyer G 2006 *Appl. Phys. A* **85** 399
[19] Rossel F, Pivetta M, Patthey F, Cávar E, Seitsonen A P and Schneider W D 2011 *Phys. Rev. B* **84** 075426
[20] Rienks E D L, Nilius N, Rust H P and Freund H J 2005 *Phys. Rev. B* **71** 241404
[21] Lin X and Nilius N 2008 *J. Phys. Chem. C* **112** 15325
[22] Nilius N, Rienks E D L, Rust H P and Freund H J 2005 *Phys. Rev. Lett.* **95** 066101
[23] Ruffieux P, Aït-Mansour K, Bendounan A, Fasel R, Patthey L, Gröning P and Gröning O 2009 *Phys. Rev. Lett.* **102** 086807
[24] Aït-Mansour K, Ruffieux P, Gröning P, Fasel R and Gröning O 2009 *J. Phys. Chem. C* **113** 5292
[25] Qin Z H, Liu C D, Chen J, Guo Q M, Yu Y H and Cao G Y 2012 *J. Chem. Phys.* **136** 024701
[26] Li H I, Franke K J, Pascual J I, Bruch L W and Diehl R D 2009 *Phys. Rev. B* **80** 085415
[27] Takayanagi K, Tanishiro Y, Takahashi M and Takahashi S 1985 *J. Vac. Sci. Technol. A* **3** 1502
[28] Wu K, Fujikawa Y, Nagao T, Hasegawa Y, Nakayama K S, Xue Q K, Wang E G, Briere T, Kumar V, Kawazoe Y, Zhang S B and Sakurai T 2003 *Phys. Rev. Lett.* **91** 126101
[29] Vitali L, Ramsey M G and Netzer F P 1999 *Phys. Rev. Lett.* **83** 316
[30] Hibino H and Ogino T 1997 *Phys. Rev. B* **55** 7018
[31] Yoon M, Lin X F, Chizhov I, Mai H A and Willis R F 2001 *Phys. Rev. B* **64** 085321
[32] Lin X F, Chizhov I, Mai H A and Willis R F 1996 *Surf. Sci.* **366** 51
[33] Custance O, Brihuega I, Gómez-Rodríguez J M and Baró A M 2001 *Surf. Sci.* **482** 1406
[34] Zhang Y P, Yang L, Lai Y H, Xu G Q and Wang X S 2003 *Surf. Sci.* **531** L378
[35] Voigtländer B and Weber T 1996 *Phys. Rev. Lett.* **77** 3861
[36] Voigtländer B 2001 *Surf. Sci. Rep.* **43** 127
[37] Chizhov I, Lee G and Willis R F 1997 *Phys. Rev. B* **56** 12316
[38] Sonnet Ph, Stauffer L and Minot C 1998 *Surf. Sci.* **407** 121
[39] Gómez-Rodríguez J M, Sáenz J J, BaróA M, Veuillen J Y and Cinti R C 1996 *Phys. Rev. Lett.* **76** 799
[40] Custance O, Brochard S, Brihuega I, Artacho E, Soler J M, BaróA M and Gómez-Rodríguez J M 2003 *Phys. Rev. B* **67** 235410
[41] Sekiguchi T, Yoshida S, Itoh K M, Mysliveček J and Voigtländer B 2007 *Appl. Phys. Lett.* **90** 013108
[42] Ansari Z A, Tomitori M and Arai T 2006 *Appl. Phys. Lett.* **88** 171902
[43] Suzuki M, Negishi R and Shigeta Y 2005 *Phys. Rev. B* **72** 235325
[44] Zhang Y P, Yan L, Xie S S, Pang S J and Gao H J 2002 *Surf. Sci.* **497** L60
[45] Motta N 2002 *J. Phys.: Condens. Matter* **14** 8353
[46] Guo H M, Wang Y L, Liu H W, Ma H F, Qin Z H and Gao H J 2004 *Surf. Sci.* **561** 227
[47] Zhao A, Zhang X, Chen G, Loy M M T and Xiao X 2006 *Phys. Rev. B* **74** 125301
[48] Köhler U, Jusko O, Pietsch G, Müller B and Henzler M 1991 *Surf. Sci.* **248** 321
[49] Wang Y L, Gao H J, Guo H M, Wang S and Pantelides S T 2005 *Phys. Rev. Lett.* **94** 106101
[50] Wang Y L, Guo H M, Qin Z H, Ma H F and Gao H J 2008 *J. Nanomater.* 874213
[51] Ma H F, Qin Z H, Xu M C, Shi D X, Gao H J, Wang S W and Pantelides S T 2007 *Phys. Rev. B* **75** 165403
[52] Qin Z H, Shi D X, Ma H F, Gao H J, Rao A S, Wang S W and Pantelides S T 2007 *Phys. Rev. B* **75** 085313
[53] Suzuki M and Shigeta Y 2003 *Surf. Sci.* **539** 113
[54] Shimada W and Tochihara H 1994 *Surf. Sci.* **311** 107
[55] Paul N, Filimonov S, Cherepanov V, Çakmak M and Voigtländer B 2007 *Phys. Rev. Lett.* **98** 166104
[56] Sun S, Murray C B, Weller D, Folks L and Moser A 2000 *Science* **287** 1989
[57] Qin Z H, Shi D X and Gao H J 2008 *Chin. Phys. B* **17** 4580
[58] Sato T, Iwatsuki T and Tachihara H 1999 *J. Electron. Microsc.* **48** 1
[59] Dou R F, Jia J F, Xu M J, Pan M H, He K, Zhang L J and Xue Q K 2004 *Acta Phys. Sin.* **53** 871 (in Chinese)
[60] Kondo Y and Takayanagi K 2000 *Science* **289** 606
[61] Li J L, Liang X J, Jia J F, Liu X, Wang J Z, Wang E G and Xue Q K 2001 *Appl. Phys. Lett.* **79** 2826
[62] Wang J, Li M and Altman E I 2004 *Phys. Rev. B* **70** 233312
[63] Oncel N, van Houselt A, Huijben J, Hallbäck A S, Gurlu O, Zandvliet H J W and Poelsema B 2005 *Phys. Rev. Lett.* **95** 116801
[64] Gurlu O, Adam O A O, Zandvliet H J W and Poelsema B 2003 *Appl. Phys. Lett.* **83** 4610
[65] Gai Z, Ji H, He Y, Hu C, Zhao R G and Yang W S 1995 *Surf. Sci.* **338** L851
[66] Bottomley D J, Iwami M, Uehara Y and Ushioda S 1999 *J. Vac. Sci. Technol. B* **17** 12
[67] Falkenberg G, Seehofer L and Johnson R L 1997 *Surf. Sci.* **371** 86
[68] Rich D H, Miller T and Chiang T C 1990 *Phys. Rev. B* **41** 3004
[69] Falkenberg G, Bunk O, Johnson R L, Rodriguez J A and Takeuchi N 2002 *Phys. Rev. B* **66** 035305
[70] Seehofer L, Falkenberg G and Johnson R L 1996 *Surf. Sci.* **352** 425
[71] Nielsen M, Smilgies D M, Feidenhans R, Landemark E, Falkenberg G, Lottermoser L, Seehofer L and Johnson R L 1996 *Surf. Sci.* **352** 430
[72] Qin Z H, Shi D X, Pang S J and Gao H J 2008 *Chin. Phys. B* **17** 1055
[73] Kevan S D 1985 *Phys. Rev. B* **32** 2344
[74] Libuda J and Freund H J 2005 *Surf. Sci. Rep.* **57** 157
[75] Tauster S J, Fung S C and Garten R L 1978 *J. Am. Chem. Soc.* **100** 170
[76] Knözinger H and Taglauer E 1997 *in Handbook of Heterogeneous Catalysis* (Weinheim, Germany: VCH) p. 216
[77] Qin Z H, Lewandowski M, Sun Y N, Shaikhutdinov S and Freund H J 2008 *J. Phys. Chem. C* **112** 10209
[78] Qin Z H, Lewandowski M, Sun Y N, Shaikhutdinov S and Freund H J 2009 *J. Phys.: Condens. Matter* **21** 134019
[79] Weiss W and Ranke W 2002 *Prog. Surf. Sci.* **70** 1
[80] Vurens G H, Maurice V, Salmeron M and Somorjai G A 1992 *Surf. Sci.* **268** 170
[81] Wulff G Z 1901 *Kristallografiya* **34** 449
[82] Hansen K H, Worren T, Stempel S, Lægsgaard E, Bäumer M, Freund H J, Besenbacher F and Stensgaard I 1999 *Phys. Rev. Lett.* **83** 4120
[83] Vitos L, Ruban A, Skriver H and Kollár J 1998 *Surf. Sci.* **411** 186
[84] Staudt T, Desikusumastuti A, Happel M, Vesselli E, Baraldi A, Gardonio S, Lizzit S, Rohr F and Libuda J 2008 *J. Phys. Chem. C* **112** 9835
[85] Desikusumastuti A, Laurin M, Happel M, Qin Z H, Shaikhutdinov S and Libuda J 2008 *Catal. Lett.* **121** 311
[86] Desikusumastuti A, Qin Z H, Staudt T, Happel M, Lykhach Y, Laurin M, Shaikhutdinov S and Libuda J 2008 *Surf. Sci.* **603** L9
[87] Desikusumastuti A, Qin Z H, Happel M, Staudt T, Lykhach Y, Laurin M, Rohr F, Shaikhutdinov S and Libuda J 2009 *Phys. Chem. Chem. Phys.* **11** 2514
[88] Desikusumastuti A, Staudt T, Qin Z H, Happel M, Laurin M, Lykhach Y, Shaikhutdinov S, Rohr F and Libuda J 2008 *Chem. Phys. Chem.* **9** 2191
[89] Desikusumastuti A, Happel M, Qin Z H, Staudt T, Lykhach Y, Laurin M, Shaikhutdinov S, Rohr F and Libuda J 2009 *J. Phys. Chem. C* **113** 9755
[90] Street S C, Xu C and Goodman D W 1997 *Annu. Rev. Phys. Chem.* **48** 43
[91] Bäumer M and Freund H J 1999 *Prog. Surf. Sci.* **61** 127
[92] Becker C, Rosenhahn A, Wiltner A, von Bergmann K, Schneider J, Pervan P, Milun M, Kralj M and Wandelt K 2002 *New J. Phys.* **4** 75
[93] Galloway H C, Benítez J J and Salmeron M 1993 *Surf. Sci.* **298** 127
[94] Ranke W, Ritter M and Weiss W 1999 *Phys. Rev. B* **60** 1527
[95] Ritter M, Ranke W and Weiss W 1998 *Phys. Rev. B* **57** 7240
[96] Rienks E D L, Nilius N, Freund H J, Giordano L, Pacchioni G and Goniakowski J 2009 *Phys. Rev. B* **79** 075427
[97] Giordano L, Pacchioni G, Goniakowski J, Nilius N, Rienks E D L and Freund H J 2007 *Phys. Rev. B* **76** 075416
[98] Binnig G, Frank K H, Fuchs H, Garcia N, Reihl B, Rohrer H, Salvan F and Williams A R 1985 *Phys. Rev. Lett.* **55** 991
[99] Bono J and Good R H Jr 1987 *Surf. Sci.* **188** 153
[100] Pivetta M, Patthey F, Stengel M, Baldereschi A and Schneider W D 2005 *Phys. Rev. B* **72** 115404
[101] Ploigt H C, Brun C, Pivetta M, Patthey F and Schneider W D 2007 *Phys. Rev. B* **76** 195404
[102] Joachim C, Gimzewski J K and Aviram A 2000 *Nature* **408** 541

[103] Joachim C, Gimzewski J K and Tang H 1998 *Phys. Rev. B* **58** 16407
[104] Harneit W 2002 *Phys. Rev. A* **65** 032322
[105] Joachim C and Gimzewski J K 1997 *Chem. Phys. Lett.* **265** 353
[106] Néel N, Kröger J and Berndt R 2006 *Adv. Mater.* **18** 174
[107] Néel N, Kröger J and Berndt R 2006 *Appl. Phys. Lett.* **88** 163101
[108] Tang L, Zhang X, Guo Q, Wu Y N, Wang L L and Cheng H P 2010 *Phys. Rev. B* **82** 125414
[109] Pai W W, Hsu C L, Lin M C, Lin K C and Tang T B 2004 *Phys. Rev. B* **69** 125405
[110] Hsu C L and Pai W W 2003 *Phys. Rev. B* **68** 245414
[111] Abel M, Dmitriev A, Fasel R, Lin N, Barth J V and Kern K 2003 *Phys. Rev. B* **67** 245407
[112] Wong S S, Pai W W, Chen C H and Lin M T 2010 *Phys. Rev. B* **82** 125442
[113] Dimitrakopoulos C D and Malenfant P R L 2002 *Adv. Mater.* **14** 99
[114] Voss D 2000 *Nature* **40** 7442
[115] Dimitrakopoulos C D, Purushothaman S, Kymissis J, Callegari A and Shaw J M 1999 *Science* **283** 822
[116] Flood A H, Stoddart J F, Steuerman D W and Heath J R 2004 *Science* **306** 2055
[117] Service R F 2001 *Science* **294** 2442
[118] Gebauer W, Bässler M, Fink R, Sokolowski M and Umbach E 1997 *Chem. Phys. Lett.* **266** 177
[119] CroneB, Dodabalapur A, Lin Y Y, Filas R W, Bao Z, LaDuca A, Sarpeshkar R, Katz H E and Li W 2000 *Nature* **403** 521
[120] Forrest S R 2004 *Nature* **428** 911
[121] Wang S, Liu Y Q, Huang X B, Yu G and Zhu D B 2003 *J. Phys. Chem. B* **107** 12639
[122] Lei S B, Deng K, Yang D L, Zeng Q D and Wang C 2006 *J. Phys. Chem. B* **110** 1256
[123] Sun Q, Wang Q, Jena P and Kawazoe Y 2005 *J. Am. Chem. Soc.* **127** 14582
[124] Stengel M, De Vita A and Baldereschi A 2003 *Phys. Rev. Lett.* **91** 166101
[125] Pai W W, Jeng H T, Cheng C M, Lin C H, Xiao X D, Zhao A D, Zhang X Q, Xu G, Shi X Q, van Hove M A, Hsue C S and Tsuei K D 2010 *Phys. Rev. Lett.* **104** 036103
[126] Li H I, Pussi K, Hanna K J, Wang L L, Johnson D D, Cheng H P, Shin H, Curtarolo S, Moritz W, Smerdon J A, McGrath R and Diehl R D 2009 *Phys. Rev. Lett.* **103** 056101
[127] Langlais V J, Schlittler R R, Tang H, Gourdon A, Joachim C and Gimzewski J K 1999 *Phys. Rev. Lett.* **83** 2809
[128] Rinaldi R, Cingolani R, Jones K M, Baski A A, Morkoc H, Di Carlo A, Widany J, Della S F and Lugli P 2001 *Phys. Rev. B* **63** 075311
[129] Proehl H, Toerker M, Fritz T, Sellam F, Leo K, Simpson Ch and Müllen K 2001 *Phys. Rev. B* **63** 205409
[130] Toerker M, Fritz T, Proehl H, Gutierrez R, Grobmann F and Schmidt R 2002 *Phys. Rev. B* **65** 245422
[131] Wachowiak A, Yamachika R, Khoo K H, Wang Y, Grobis M, Lee D H, Louie S G and Crommie M F 2005 *Science* **310** 468
[132] Silien C, Pradhan N A, Ho W and Thiry P A 2004 *Phys. Rev. B* **69** 115434
[133] Cepek C, Goldoni A and Modesti S 1996 *Phys. Rev. B* **53** 7466
[134] Pedio M, Hevesi K, Zema N, Capozi M, Perfetti P, Gouttebaron R, Pireaux J J, Caudano R and Rudolf P 1999 *Surf. Sci.* **43** 7249
[135] Cheng Z H, Gao L, Deng Z T, Liu Q, Jiang N, Lin X, He X B, Du S X and Gao H J 2007 *J. Phys. Chem. C* **111** 2656
[136] Takada M and Tada H 2004 *Chem. Phys. Lett.* **392** 265
[137] Ge X, Manzano C, Berndt R, Anger L T, Köhler F and Herges R 2009 *J. Am. Chem. Soc.* **131** 6096
[138] Chen X, Fu Y S, Ji S H, Zhang T, Cheng P, Ma X C, Zou X L, Duan W H, Jia J F and Xue Q K 2008 *Phys. Rev. Lett.* **101** 197208
[139] Zhao A D, Li Q X, Chen L, Xiang H J, Wang W H, Pan S, Wang B, Xiao X D, Yang J L, Hou J G and Zhu Q S 2005 *Science* **309** 1542
[140] Zhao A D, Hu Z P, Wang B, Xiao X D, Yang J L and Hou J G 2008 *J. Chem. Phys.* **128** 234705
[141] Aguiar-Hualde J M, Chiappe G, Louis E, Anda E V and Simonin J 2009 *Phys. Rev. B* **79** 155415
[142] Hipps K W, Lu X, Wang X D and Mazur U 1996 *J. Phys. Chem.* **100** 11207
[143] Sakurai T, Wang X D, Xue Q K, Hasegawa Y, Hashizume T and Shinohara H 1996 *Prog. Surf. Sci.* **51** 263
[144] Rosei F, Schunack M, Naitoh Y, Jiang P, Gourdon A, Laegsgaard E, Stensgaard I, Joachim C and Besenbacher F 2003 *Prog. Surf. Sci.* **71** 95
[145] Hou J G, Yang J L, Wang H Q, Li Q X, Zeng C G, Yuan L F, Wang B, Chen D M and Zhu Q S 2001 *Nature* **409** 304
[146] Hou J G, Yang J L, Wang H Q, Li Q X, Zeng C G, Lin H, Wang B, Chen D M and Zhu Q S 1999 *Phys. Rev. Lett.* **83** 3001
[147] Modesti S, Cerasari S and Rudolf P 1993 *Phys. Rev. Lett.* **71** 2469
[148] Hinterstein M, Torrelles X, Felici R, Rius J, Huang M, Fabris S, Fuess H and Pedio M 2008 *Phys. Rev. B* **77** 153412
[149] Gardener J A, Briggs G A D and Castell M R 2009 *Phys. Rev. B* **80** 235434
[150] Zhang X, Tang L and Guo Q M 2010 *J. Phys. Chem. C* **114** 6433
[151] Ogawa A, Tachibana M, Kondo M, Yoshizawa K, Fujimoto H and Hoffmann R 2003 *J. Phys. Chem. B* **107** 12672
[152] Wang L L and Cheng H P 2004 *Phys. Rev. B* **69** 045404
[153] Dutton G and Zhu X Y 2004 *J. Phys. Chem. B* **108** 7788
[154] Maxwell A J, Brühwiler P A, Arvanitis D, Hasselström J, Johansson M K J and Mårtensson N 1998 *Phys. Rev. B* **57** 7312
[155] Chen W, Zhang H L, Xu H, Tok E S, Loh K P and Wee A T S 2006 *J. Phys. Chem. B* **110** 21873
[156] Casarin M, Forrer D, Orzali T, Petukhov M, Sambi M, Tondello E and Vittadini A 2007 *J. Phys. Chem. C* **111** 9365
[157] Orzali T, Forrer D, Sambi M, Vittadini A, Casarin M and Tondello E 2008 *J. Phys. Chem. C* **112** 378
[158] Torrelles X, Langlais V, Santis M D, Tolentino H C N and Gauthier Y 2010 *J. Phys. Chem. C* **114** 15645
[159] Felici R, Pedio M, Borgatti F, Iannotta S, Capozi M, Ciullo G and Stierle A 2005 *Nat. Mater.* **4** 688
[160] Huang M 2012 *Phys. Chem. Chem. Phys.* **14** 4959